Acta Crystallographica Section A
Foundations of Crystallography
ISSN 0108-7673

Received 27 August 2005
Accepted 13 March 2006

Precise measurement of local strain fields with energy-unfiltered convergent-beam electron diffraction

Takashi Yamazaki,[a]* Tomoko Isaka,[a] Koji Kuramochi,[a] Iwao Hashimoto[a] and Kazuto Watanabe[b]

[a]Department of Physics, Tokyo University of Science, Tokyo 162-8601, Japan, and [b]Tokyo Metropolitan College of Industrial Technology, Tokyo 140-0011, Japan. Correspondence e-mail: yamazaki@rs.kagu.tus.ac.jp

A simple and robust method to precisely determine local strain fields using energy-unfiltered convergent-beam electron diffraction is presented. This method involves the subtraction of background intensity, the extraction of higher-order Laue-zone lines by tracing using a Radon transformation and a system of analytical strain determination without the need for an optimization routine such as χ^2-based minimization. As an example, the measurement of residual strain in a silicon-on-insulator wafer is demonstrated. It is found from micro-Raman spectroscopy analysis that, at the nanometre scale, this measurement succeeds with an accuracy of 0.06%.

© 2006 International Union of Crystallography
Printed in Great Britain – all rights reserved

1. Introduction

Recent advances in semiconductor technology have reduced structure sizes to the submicrometre scale (Sperars & Smith, 1972; Ogawa *et al.*, 1996; Fukuda *et al.*, 1996). This emphasis on miniaturization necessitates the elucidation of local properties of the materials used in semiconductor technology and increases the demand for measurements on the nanometre scale. Furthermore, semiconductor devices become functional through combinations of different materials, so that lattice strain is induced around the interfaces in these heterogeneous systems. In general, the strain at an interface is caused by the differences in lattice constant, thermal expansion coefficient and elastic constant between two materials. Since such strain can often lead to a breakdown of functionality, intensive theoretical and experimental studies have been carried out in order to understand its effects.

Currently, strain over an area of a few micrometres can be precisely evaluated by X-ray diffraction (Ando *et al.*, 1973; Yamamoto & Sakata, 1989), microscopic Raman spectroscopy (Wolf *et al.*, 1993) and photoluminescence spectroscopy (Shirakata *et al.*, 1986). However, these techniques have a common drawback in that their spatial resolution is limited to approximately 1 μm, which is insufficient for the investigation of strain in the latest devices. Transmission electron microscopy (TEM) has greatly contributed to local structural and compositional analysis owing to its high spatial resolution, and high-resolution TEM image processing is another technique that allows local strain to be measured (Hÿtch *et al.*, 1998; Gerthsen *et al.*, 2000; Ruterana *et al.*, 2002). High-angle annular dark-field scanning transmission electron microscopy has also succeeded in determining the local strain around the InGaN layer in multiple quantum wells InGaN/GaN (Watanabe *et al.*, 2003). However, despite their high spatial resolution, the accuracy of TEM methods is currently much lower than that of X-ray diffraction.

The only technique with the potential to provide information on the lattice strain with sufficiently high spatial resolution and accuracy may be convergent-beam electron diffraction (CBED), which uses higher-order Laue-zone (HOLZ) lines that appear in a bright-field disc. Probes with diameters of a few nanometres can easily be formed, thus CBED is well adapted to the dimensions over which strain may vary in the latest devices. Consequently, there are a growing number of studies in which this technique has been successfully applied to many materials (Rozeveld & Howe, 1993; Tomokiyo *et al.*, 1994; Wittmann *et al.*, 1998; Yonemura *et al.*, 1999; Krämer *et al.*, 2000; Uesugi *et al.*, 2000; Toda *et al.*, 2000; Akagi *et al.*, 2004). However, there are various problems inherent to the CBED technique, for example its thin-foil relaxations and dynamical scattering effects. Furthermore, since inelastic scattering gives faded HOLZ lines that make their analysis difficult, energy-filtered CBED patterns are essential for accurate studies (Spence & Zuo, 1993; Deininger *et al.*, 1994). However, energy filtering is very rarely incorporated in electron microscopes. In addition, the lack of an accurate refinement algorithm has prevented the implementation of the CBED method as a standard technique for strain measurement, although some optimized algorithms involving a χ^2-based minimization routine have already been proposed (Zuo, 1992; Krämer & Mayer, 1999).

In this paper, we report a different technique for high-precision measurements of local residual strain using energy-unfiltered CBED, which has two advantages. First, lattice

parameters are obtained at first hand without the need for a refinement process, thus the results are independent of initially specified lattice parameters. Second, this method achieves an accuracy of 0.06% even with energy-unfiltered CBED patterns, whereas an accuracy of 0.2% is generally required in practice.

2. Experimental procedure

CBED measurements of [012]-oriented Si were carried out because they yielded a sufficient number of intense HOLZ lines and the kinematical approximation is appropriate. A silicon-on-insulator (SOI) wafer was used in this study, comprised of a sandwich structure of a 50 μm thick *n*-type Si(100) layer with a resistivity of 10 Ω cm, a 500 nm thick buried oxide (BOX) layer and an *n*-type Si(100) substrate. It was fabricated by a bonded method. In order to obtain the CBED patterns of Si(012), specimens were prepared as follows. Si chips were pasted onto each side of the SOI wafer for reinforcement and were cut into 18° oriented slabs. The samples were mechanically thinned and polished to a thickness of approximately 20 μm by using a dimple grinder. Final thinning was carefully carried out by means of 4 keV Ar^+ ion milling at an angle of 4°. CBED patterns were obtained using a HITACH H-9000NAR electron microscope operated at 200 keV with a 10 nm probe and an LaB_6 filament. All measurements were performed at room temperature.

Micro-Raman spectroscopy was carried out using a Ramanor U-1000 (Jobin Yvon) operated at 5 mW Ar^+ laser with an excitation wavelength of 457.9 nm. The radius of the focused laser beam was 500 nm. Micro-Raman spectra of both sides of the wafer, taken at points 500 nm away from the interfaces, are shown in Fig. 1. The side of the Si substrate has a slight tensile stress and that of the Si overlay has a compressive stress.

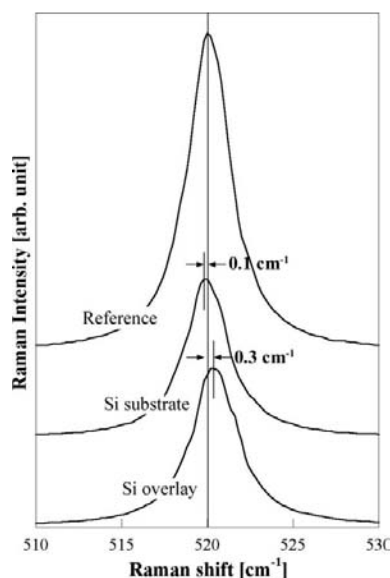

Figure 1
Raman spectra of both sides of the SOI wafer taken at points 500 nm away from the $Si–SiO_2$ interfaces, together with the reference spectrum.

3. Methods

Before obtaining the local lattice parameters, it is necessary to determine the accelerating voltage accurately using a reference CBED pattern taken at a stress-free region. The raw experimental CBED pattern is shown in Fig. 2(*a*). The method by which HOLZ lines are traced is outlined below.

3.1. Background subtraction and tracing HOLZ lines by Radon transformation

In order to determine local strain, it is necessary to extract the straight HOLZ lines from an experimental CBED pattern with high precision. However, it is difficult to directly trace HOLZ lines from raw CBED patterns owing to the noise, and the high intensity distribution, of the background. The background intensity distribution, which has to be subtracted initially, gradually decreases from the centre of the CBED disc. Therefore, the background intensity must be eliminated by a Fourier filtering method, in which a mask is applied to the central spot in Fourier space. The background-subtracted reference CBED pattern, where the optimum mask size was used, is shown in Fig. 2(*b*). Notably, both the second-order Laue-zone lines and the first-order Laue-zone (FOLZ) lines can clearly be visualized by this simple approach. Black masks are then applied to the intersections of the HOLZ lines, as shown in Fig. 2(*c*), because the HOLZ lines near the inter-

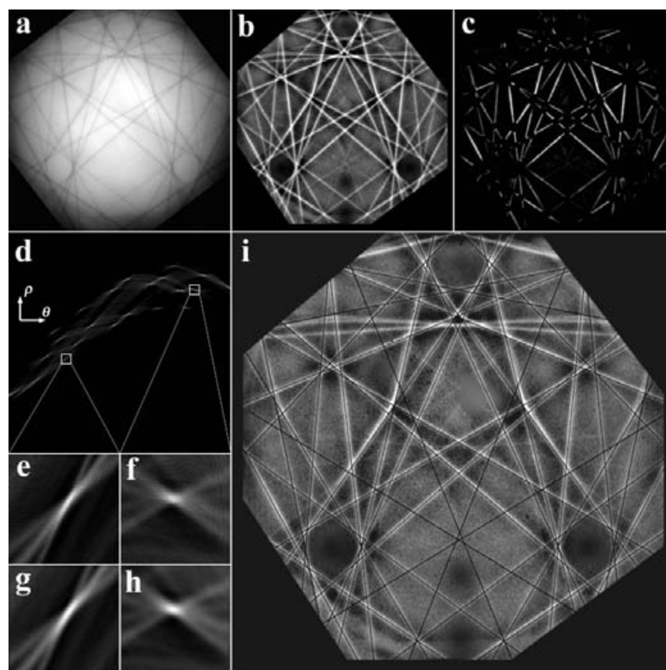

Figure 2
(*a*) Experimental energy-unfiltered CBED pattern of a [012]-oriented Si substrate from a stress-free region, (*b*) image with the background intensity subtracted, (*c*) image in which black masks are applied at all intersections of two HOLZ lines. (*c*) is used for the initial image. (*d*) Transformed space image calculated by Radon transformation of (*c*). (*e*) and (*f*) Enlarged images of two bright spots, used as examples, (*g*) and (*h*) their corresponding noise-filtered images. (*i*) Image formed by superimposing all traced HOLZ lines on (*b*).

sections are bent by dynamical effects (Krämer & Mayer, 1999).

In recent years, the Hough and Radon transformations have been used to automatically extract straight HOLZ lines, where a discrete Radon transformation corresponds to the Hough transformation (Hough, 1962; Zuo, 1992; Toft, 1996; Krämer & Mayer, 1999; Krämer *et al.*, 2000). These two methods are standard tools in image analysis that allow the recognition of a whole pattern in image space from a local pattern in transformed space. We use the Radon transformation in the present investigation:

$$R(\theta,\rho)=\int_{-\infty}^{\infty}\int_{-\infty}^{\infty} f(x,y)\delta(\rho - x\cos\theta - y\sin\theta)\,\mathrm{d}x\mathrm{d}y, \quad (1)$$

where $f(x, y)$ is the image intensity at (x, y). The Radon transformation converts image space (x, y) into transformed space (ρ, θ), in which each point corresponds to a straight line in image space. The positions of the strong spots in transformed space are coupled to the parameters of the straight lines in image space. The transformation of the image in Fig. 2(*c*) is displayed in Fig. 2(*d*), where maxima are apparent as strong bright spots. By way of illustration, enlarged images of the two spots enclosed by white squares in Fig. 2(*d*) are shown in Figs. 2(*e*) and 2(*f*). Since the experimental image contains a distribution of intensities and noise, transformed space also becomes noisy. In order to find the exact maxima, the Fourier filtering method, in which the central spot in Fourier space is covered by a mask, is applied. The noise-filtered images corresponding to Figs. 2(*e*) and 2(*f*) are shown in Figs. 2(*g*) and 2(*h*), respectively. The image formed by superimposing on Fig. 2(*b*) all of the HOLZ lines obtained from the maxima in transformed space is displayed in Fig. 2(*i*), where the quality of the match confirms that the Radon transformation has the capacity to extract straight HOLZ lines.

The error of tracing HOLZ lines is influenced by the resolution of an experimental image and the resolution of transformed space. The resolution of transformed space can be enlarged theoretically so that subpixel analysis is attained in Radon transformation (Krämer *et al.*, 2000). In the present analysis, the central disc of an experimental image is taken in as a digital image of 1024×1024 pixels by image scanner. Furthermore, the resolution of transformed space is calculated by 4096×4096 pixels. The error of tracing HOLZ lines was estimated using the dynamical simulated image. As a result, it is found that tracing HOLZ lines is performed within the error of ± 0.5 pixels.

3.2. Analytical determination of local lattice parameters

Under the kinematical approximation, HOLZ lines of an *hkl* reflection are given by

$$K_y = -\frac{g_x}{g_y}K_x + \frac{g_z}{g_y}W - \frac{g^2}{2g_y}, \quad (2)$$

where K_x and K_y are projections of the wavevector onto the coordinate axes x and y of the diffraction plane, and W is the wavenumber corresponding to the effective accelerating voltage. In the case of a triclinic system, g_x, g_y and g_z are given by

$$\begin{cases} g_x = \dfrac{h}{a\sin\beta} - \dfrac{Z\cos\beta}{c\sin\beta} \\ g_y = -\dfrac{hX}{aY\sin\beta} + \dfrac{k}{Y} - \dfrac{(Z\sin\beta - X\cos\beta)}{Yc\sin\beta} \\ g_z = \dfrac{l}{c} \\ X = \dfrac{b(\cos\gamma - \cos\alpha\cos\beta)}{\sin\beta} \\ Y = \dfrac{b}{\sin\beta}[\sin^2\alpha\sin^2\beta - (\cos\alpha\cos\beta - \cos\gamma)^2]^{1/2} \\ Z = \cos\alpha. \end{cases}$$

From these equations, the coordinate of the intersection between two HOLZ lines corresponding to hkl and $h'k'l'$ reflections is easily calculable. Under the assumption of a small strain field, the shift of this intersection can be analytically calculated by the Taylor expansion:

$$\begin{aligned}
\Delta K_x = {} & \frac{1}{2(hk'-h'k)}\bigg\{\bigg[k'\bigg(2\frac{l}{c}W - \frac{h^2}{a^2} - \frac{k^2}{b^2} - \frac{l^2}{c^2}\bigg) \\
& - k\bigg(2\frac{l'}{c}W - \frac{h'^2}{a^2} - \frac{k'^2}{b^2} - \frac{l'^2}{c^2}\bigg)\bigg] + \frac{1}{a^2}(h^2k' - h'^2k)\bigg\}\Delta a \\
& + \frac{akk'}{b^3(hk'-h'k)}(k-k')\Delta b \\
& + \frac{a}{2(hk'-h'k)}\bigg[\frac{1}{c^3}(k'l^2 - kl'^2) + \frac{W}{c^2}(kl' - k'l)\bigg]\Delta c \\
& + \frac{1}{2c(hk'-h'k)}\bigg\{ab\bigg[l'\bigg(2\frac{l}{c}W - \frac{h^2}{a^2} - \frac{k^2}{b^2} - \frac{l^2}{c^2}\bigg) \\
& - l\bigg(2\frac{l'}{c}W - \frac{h'^2}{a^2} - \frac{k'^2}{b^2} - \frac{l'^2}{c^2}\bigg)\bigg] \\
& - \frac{ab(hl'-h'l)}{hk'-h'k}\bigg[k'\bigg(2\frac{l}{c}W - \frac{h^2}{a^2} - \frac{k^2}{b^2} - \frac{l^2}{c^2}\bigg) \\
& - k\bigg(2\frac{l'}{c}W - \frac{h'^2}{a^2} - \frac{k'^2}{b^2} - \frac{l'^2}{c^2}\bigg)\bigg] + \frac{2kk'(l'-l)}{b}\bigg\}\Delta\alpha \\
& + \frac{1}{c(hk'-h'k)}\bigg\{(h'kl' - hk'l) - \frac{a^2(k'l - kl')}{2(hk'-h'k)} \\
& \times\bigg[k'\bigg(2\frac{l}{c}W - \frac{h^2}{a^2} - \frac{k^2}{b^2} - \frac{l^2}{c^2}\bigg) \\
& - k\bigg(2\frac{l'}{c}W - \frac{h'^2}{a^2} - \frac{k'^2}{b^2} - \frac{l'^2}{c^2}\bigg)\bigg]\bigg\}\Delta\beta \\
& + \frac{1}{hk'-h'k}\bigg\{\frac{b}{2}\bigg[h'\bigg(2\frac{l}{c}W - \frac{h^2}{a^2} - \frac{k^2}{b^2} - \frac{l^2}{c^2}\bigg) \\
& - h\bigg(2\frac{l'}{c}W - \frac{h'^2}{a^2} - \frac{k'^2}{b^2} - \frac{l'^2}{c^2}\bigg)\bigg] + \frac{kk'(h'-h)}{b}\bigg\}\Delta\gamma, \quad (3)
\end{aligned}$$

$$\begin{aligned}\Delta K_y = {} & \frac{bhh'}{a^3(h'k-hk')}(h-h')\Delta a \\ & + \frac{1}{2(h'k-hk')}\left\{\left[h'\left(2\frac{l}{c}W - \frac{h^2}{a^2} - \frac{k^2}{b^2} - \frac{l^2}{c^2}\right)\right.\right. \\ & \left.\left. - h\left(2\frac{l'}{c}W - \frac{h'^2}{a^2} - \frac{k'^2}{b^2} - \frac{l'^2}{c^2}\right)\right] + \frac{1}{b^2}(h'k^2 - hk'^2)\right\}\Delta b \\ & + \frac{b}{2(h'k-hk')}\left[\frac{1}{c^3}(h'l^2 - hl'^2) + \frac{W}{c^2}(hl' - h'l)\right]\Delta c \\ & + \frac{1}{c(h'k-hk')}\left\{(hk'l' - h'kl) - \frac{b^2(h'l-hl')}{2(h'k-hk')}\right. \\ & \times \left[h'\left(2\frac{l}{c}W - \frac{h^2}{a^2} - \frac{k^2}{b^2} - \frac{l^2}{c^2}\right)\right. \\ & \left.\left. - k\left(2\frac{l'}{c}W - \frac{h'^2}{a^2} - \frac{k'^2}{b^2} - \frac{l'^2}{c^2}\right)\right]\right\}\Delta\alpha \\ & + \frac{1}{2c(h'k-hk')}\left\{ab\left[l'\left(2\frac{l}{c}W - \frac{h^2}{a^2} - \frac{k^2}{b^2} - \frac{l^2}{c^2}\right)\right.\right. \\ & \left. - l\left(2\frac{l'}{c}W - \frac{h'^2}{a^2} - \frac{k'^2}{b^2} - \frac{l'^2}{c^2}\right)\right] \\ & - \frac{ab(kl'-k'l)}{h'k-hk'}\left[h'\left(2\frac{l}{c}W - \frac{h^2}{a^2} - \frac{k^2}{b^2} - \frac{l^2}{c^2}\right)\right. \\ & \left.\left. - k\left(2\frac{l'}{c}W - \frac{h'^2}{a^2} - \frac{k'^2}{b^2} - \frac{l'^2}{c^2}\right)\right] + \frac{2hh'(l'-l)}{a}\right\}\Delta\beta \\ & + \frac{hh'(k'-k)}{a(h'k-hk')}\Delta\gamma, \end{aligned} \tag{4}$$

where the higher-order terms of Δa, Δb, Δc, $\Delta\alpha$, $\Delta\beta$ and $\Delta\gamma$ are neglected only when the strain field is very small. In this way, the shift of intersections of HOLZ lines can be approximated with a linear function for each lattice parameter, although an actual shift is given by a non-linear equation of six lattice parameters.

Some researchers (Toda *et al.*, 2000; Akagi *et al.*, 2004) have proposed methods of analysing CBED patterns by considering only those HOLZ lines that are sensitive to the lattice parameters. They assumed that HOLZ reflections are insensitive to the lattice parameters associated with the direction parallel to the incident electron beam and sensitive to those associated with the direction perpendicular to the beam. In the present coordinate system, the c axis coincides with the incident direction, which is of great advantage in selecting the HOLZ lines that are sensitive to small lattice strains. For our samples, the a, b and c axes are set to the [100], $[02\bar{1}]$ and [012] directions. The case where no strain is present is the tetragonal system, where $a = 5.431$, $b = 5.431\times\sqrt{5}$, $c = 5.431\times\sqrt{5}$ nm and $\alpha = \beta = \gamma = 90^\circ$. In the present configuration, it is found that the coefficients of the linear equations containing $\Delta\alpha$ and $\Delta\beta$ are very small compared to those containing Δa, Δb, Δc and $\Delta\gamma$. This implies that only four lattice parameters, Δa, Δb, Δc and $\Delta\gamma$, can be determined. As for comparison with the experimental data, four ratios of the distances between intersections of HOLZ lines, e_1, e_2, e_3 and e_4, are used. The set of equations involving the four ratios is represented as follows:

$$\begin{pmatrix} C_{11} & C_{12} & C_{13} & C_{14} \\ C_{21} & C_{22} & C_{23} & C_{24} \\ C_{31} & C_{32} & C_{33} & C_{34} \\ C_{41} & C_{42} & C_{43} & C_{44} \end{pmatrix}\begin{pmatrix} \Delta a \\ \Delta b \\ \Delta c \\ \Delta\gamma \end{pmatrix} = \begin{pmatrix} e_1 \\ e_2 \\ e_3 \\ e_4 \end{pmatrix}$$

$$\mathbf{C}\cdot\mathbf{\Delta}S = \mathbf{E}, \tag{5}$$

where C_{ij} are the coefficients obtained by the Taylor expansion. By using equation (5), the four unknown lattice parameters can be determined analytically.

If four equations are used then the number of equations and unknowns is the same and there is a good chance of a solution providing a unique set of lattice parameters. However, there is no unique solution if one or more of the four equations are linear combinations of the others, or if all equations contain certain variables in exactly the same linear combination. These considerations necessitate the calculation of the determinant of the matrix constructed by coefficients of the unknown parameters. A unique solution cannot be calculated if the determinant is zero. Unfortunately, even if all combinations of HOLZ lines in this orientation are taken, the determinant of equation (5) becomes 0. In this case, it is impossible to determine four lattice parameters independently. Krämer *et al.* (2000) discussed this problem in detail and used the volume calculated by the finite element method as the third equation. In the present case, $\Delta b = \Delta c$ is assumed owing to the symmetry of the sample and this relationship can be used as the third equation. Therefore, the set of equations to be solved is rewritten as:

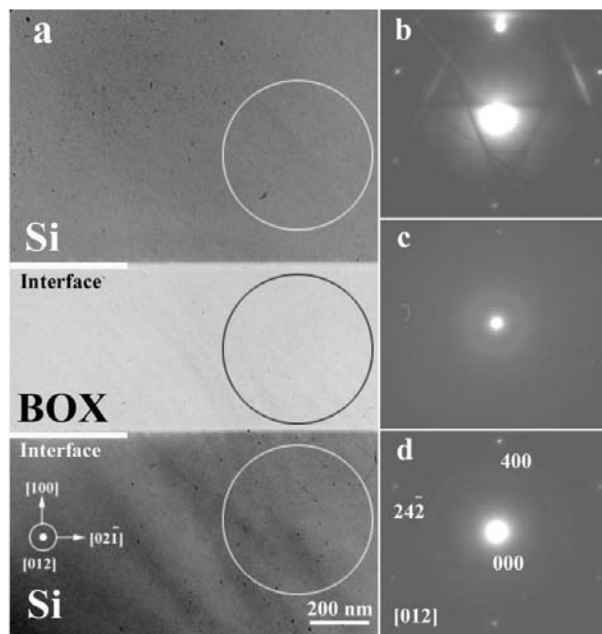

Figure 3
Cross-sectional bright-field TEM image of SOI wafer. White lines denote the positions of Si/SiO_2 interfaces. Upper, central and lower regions correspond to the Si overlay, BOX, and Si substrate, respectively. The CBED patterns were obtained with the incident electron beam parallel to [012].

$$\begin{pmatrix} C_{11} & C_{12} & C_{13} & C_{14} \\ C_{21} & C_{22} & C_{23} & C_{24} \\ 0 & 1 & -1 & 0 \\ C_{41} & C_{42} & C_{43} & C_{44} \end{pmatrix} \begin{pmatrix} \Delta a \\ \Delta b \\ \Delta c \\ \Delta \gamma \end{pmatrix} = \begin{pmatrix} e_1 \\ e_2 \\ 0 \\ e_4 \end{pmatrix}$$

$$\mathbf{C}' \cdot \mathbf{\Delta} S = \mathbf{E}'. \qquad (6)$$

In order to obtain high measurement accuracy, it is necessary to select the appropriate HOLZ lines. It is found that the errors are reduced when combinations of HOLZ lines that give a large determinant of $\mathbf{C}'$ are selected. In practice, many combinations having large determinants of $\mathbf{C}'$ are used (584 sets of combinations of HOLZ lines were actually used). The fluctuations of the solutions that are averaged give rise to the measured error. The accuracy does not depend only on the measurement accuracy of one e_i. The total error consists of a relative error and an absolute error. The relative error due to tracing HOLZ lines is estimated to be 0.05% in the present experiment. In addition, the absolute error due to the effective accelerating voltage is determined to be 0.01% from the comparison between the experimental image and simulated results at the stress-free region. Another factor that contributes to the absolute error is the thickness dependence of the positions of HOLZ lines (Mansfield *et al.*, 1993). Fortunately, this factor is not important if the dynamical effect is very small as in the present orientation. Therefore, the error due to the thickness dependence can be neglected. As a result, the final error has been estimated as 0.06%.

4. Results and discussion

Fig. 3(*a*) shows a cross-sectional bright-field TEM image of the Si overlay, BOX, and Si substrate that comprise the SOI wafer. Selected-area diffraction (SAD) patterns taken from each region are displayed in Figs. 3(*b*)–(*d*). The positions of the selected-area aperture are shown by large circles in Fig. 3(*a*). A diffuse ring due to amorphous SiO_2 can be seen in Fig. 3(*c*). It is noted that the Si overlay and the Si substrate are slightly misoriented because the SOI wafer was made by the bonded method.

CBED patterns were taken at various points across the Si–SiO_2 interfaces. The effective acceleration voltage was determined using a reference image taken from the region which was 10 µm or more away from the interface. For illustration, the raw CBED patterns observed at distances of 5.0 and 2.0 µm from the interface between the BOX layer and the Si substrate are displayed in Figs. 4(*a*)–(*b*). In addition, the raw CBED pattern observed at distances of 2.0 µm from the interface between the BOX layer and the Si overlay is displayed in Fig. 4(*c*). The exact positions of the measurements were determined from the traces of the contamination due to the exposures on the sample. Although raw CBED patterns become ambiguous close to the interface, strong FOLZ lines are visible. In Figs. 4(*d*)–(*f*), the FOLZ lines traced by the method described above are superimposed on the background-subtracted images. The central areas enclosed by the white boxes in Figs. 4(*d*)–(*f*) are shown in greater detail in Figs. 4(*g*)–(*i*).

The local lattice parameters were determined for the three CBED patterns shown in Fig. 4. In order to confirm the validity of these values, the CBED patterns were simulated

Figure 4
(*a*), (*b*) Raw CBED patterns obtained at distances of 1.0 and 2.0 µm from the interface between the BOX layer and the Si substrate. (*c*) Raw CBED pattern obtained at a distance of 2.0 µm from the interface between the BOX layer and the Si overlay. (*d*)–(*f*) Images in which HOLZ lines traced by the present method are superimposed on the patterns in (*a*)–(*c*) after background subtraction. (*g*)–(*i*) Corresponding enlarged images of the regions outlined by white boxes in (*d*)–(*f*).

using dynamical theory, where the lattice parameters determined by the present method were used. The experimental CBED patterns which superimpose the dynamical simulated results are shown in Figs. 5(*a*)–(*c*). It is found that the HOLZ lines obtained by dynamical simulation are perfectly superimposed on the experimental CBED patterns, implying that these images can be sufficiently approximated by kinematical theory.

The distribution of residual strain components as a function of the distance from the SiO_2/Si interfaces is presented in Figs. 6(*a*)–(*c*), where the vertical grey band represents the position of the BOX layer. The results of the micro-Raman method are also displayed in Fig. 6(*d*). The side of the wafer containing the Si substrate has a slight tensile stress and that of the Si overlay has a compressive stress, although there is almost no shear stress. Consequently, it is found that the residual stress of the SOI wafer is normal stress. The stress on both sides of the wafer increases towards the Si/SiO_2 interface. The good agreement between the results obtained from the CBED and micro-Raman methods leads to the conclusion that the validity of the CBED method is clearly substantiated.

5. Conclusions

A simple and robust method is proposed to accurately determine local strain fields from energy-unfiltered CBED patterns. This method involves the subtraction of background intensity, the extraction of HOLZ lines by tracing using a

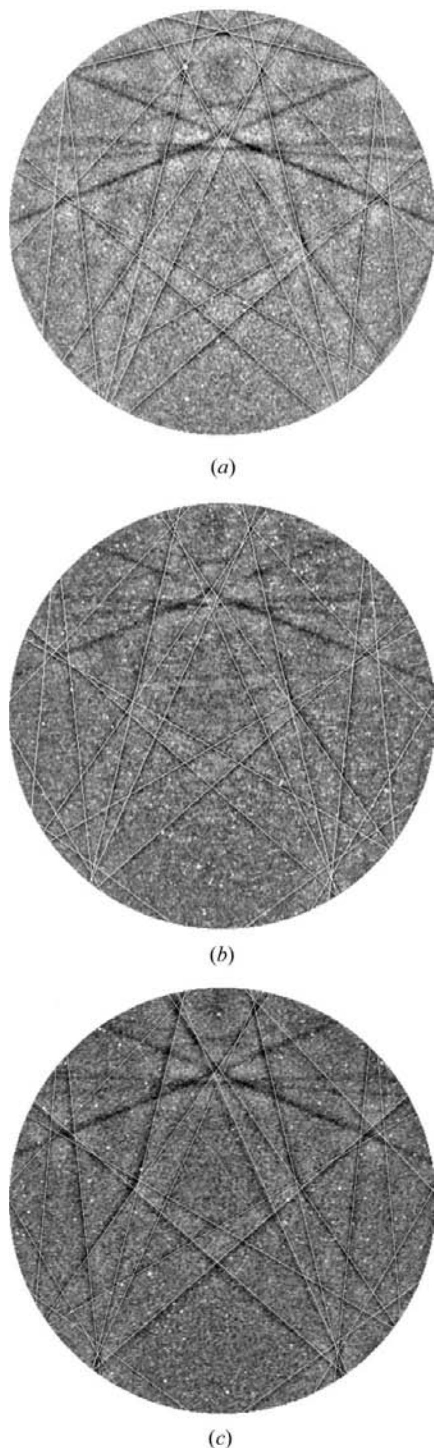

Figure 5
(*a*)–(*c*) Dynamical simulated CBED patterns superimposed on the background-subtracted experimental CBED patterns in Figs. 4(*d*)–(*f*).

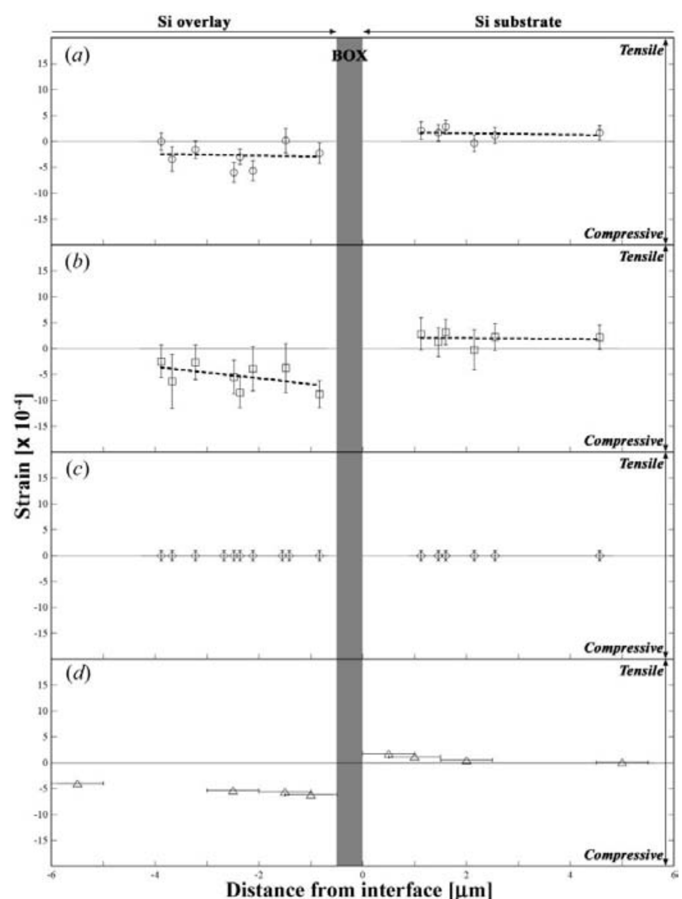

Figure 6
(*a*)–(*c*) The distribution of strain components *a*, *b* and γ as a function of distance from the Si/SiO_2 interface in the SOI wafer and (*d*) the distribution of strain measured by micro-Raman spectroscopy. The vertical gray band denotes the position of the BOX layer. In (*d*), lateral error bars express the diameter of the laser beam.

Radon transformation and a system of analytical strain determination without the need for an optimization process such as χ^2-based minimization. The process is demonstrated by studying the strain in [012]-oriented Si across the SiO_2/Si interface in a SOI wafer. The results are compared with those from micro-Raman spectroscopy, and the CBED method achieves an accuracy level above 0.06% even when energy-unfiltered CBED is used. This method can immediately be applied to other materials of any crystal symmetry without the need for prior assumptions of lattice parameters.

This research was partially supported by the Kazato Research Foundation. This research was partially supported by the Ministry of Education, Science, Sports and Culture, Grant-in-Aid for Scientific Research (C), 15560024, 2003.

References

Akagi, T., Tsuda, K., Terauchi, M. & Tanaka, M. (2004). *J. Electron Microsc.* **53**, 11–19.
Ando, Y., Patel, J. R. & Kato, N. (1973). *J. Appl. Phys.* **44**, 4405–4412.
Deininger, C., Necker, G. & Mayer, J. (1994). *Ultramicroscopy*, **41**, 211–223.
Fukuda, M., Endo, N., Tsuyuzaki, H., Suzuki, M. & Deguchi, K. (1996). *Jpn. J. Appl. Phys.* **35**, 6458–6462.
Gerthsen, D., Hahn, E., Neubauer, B., Rosenauer, A., Schön, M. H. & Rizzi, A. (2000). *Phys. Status Solidi A*, **177**, 145–155.
Hough, P. V. C. (1962). US Patent 3069654.
Hÿtch, M. J., Snoeck, E. & Kilaas, R. (1998). *Ultramicroscopy*, **74**, 131–146.
Krämer, S. & Mayer, J. (1999). *J. Microsc.* **194**, 2–11.
Krämer, S., Mayer, J., Witt, C., Weickenmeier, A. & Rühle, M. (2000). *Ultramicroscopy*, **81**, 245–262.
Mansfield, J., Bird, D. & Saunders, M. (1993). *Ultramicroscopy*, **48**, 1–11.
Ogawa, T., Sekiguchi, A. & Yoshizawa, N. (1996). *Jpn. J. Appl. Phys.* **35**, 6360–6365.
Rozeveld, S. J. & Howe, J. M. (1993). *Ultramicroscopy*, **50**, 41–56.
Ruterana, P., Kret, S., Vivet, A., Maciejewski, G. & Dluzewski, P. (2002). *J. Appl. Phys.* **91**, 8979–8985.
Shirakata, S., Fujiwara, Y., Kondo, M., Nishino, T. & Hamakawa, Y. (1986). *J. Electron. Mater.* **15**, 323–329.
Spence, J. C. H. & Zuo, J. M. (1993). *Electron Microdiffraction.* New York: Plenum Press.
Sperars, D. L. & Smith, H. (1972). *Electron Lett.* **8**, 102–105.
Toda, A., Ikarashi, N. & Ono, H. (2000). *J. Crystal Growth*, **210**, 341–345.
Toft, P. (1996). *The Radon Transform – Theory and Implementation.* PhD thesis, Department of Mathematical Modeling, Technical University of Denmark, Lyngby, Denmark.
Tomokiyo, Y., Matsuhata, S., Okuyama, T., Yasunaga, T., Kuwano, N. & Oki, K. (1994). *Ultramicroscopy*, **54**, 276–285.
Uesugi, F., Kikuchi, Y., Watanabe, K. & Hashimoto, I. (2000). *Phys. Status Solidi A*, **177**, 331–339.
Watanabe, K., Nakanishi, N., Yamazaki, T., Yang, J. R., Huang, S. Y., Inoke, K., Htsu, J. T., Tu, R. C. & Shiojiri, M. (2003). *Appl. Phys. Lett.* **82**, 715–717.
Wittmann, R., Parzinger, C. & Gerthsen, D. (1998). *Ultramicroscopy*, **70**, 145–159.
Wolf, I. D., Norstrom, H. & Maes, H. E. (1993). *J. Appl. Phys.* **74**, 4490–4500.
Yamamoto, N. & Sakata, S. (1989). *Jpn. J. Appl. Phys.* **28**, L2065–L2068.
Yonemura, M., Sueoka, K. & Kamei, K. (1999). *Jpn. J. Appl. Phys.* **38**, 3440–3447.
Zuo, J. M. (1992). *Ultramicroscopy*, **41**, 211–223.